Probing and Manipulating Valley Coherence of Dark Excitons in Monolayer WSe_2

M. R. Molas,[1,2,*] A. O. Slobodeniuk,[1] T. Kazimierczuk,[2] K. Nogajewski,[1,2] M. Bartos,[1]
P. Kapuściński,[1,3] K. Oreszczuk,[2] K. Watanabe,[4] T. Taniguchi,[4] C. Faugeras,[1]
P. Kossacki,[2] D. M. Basko,[5] and M. Potemski[1,2,†]

[1]*Laboratoire National des Champs Magnétiques Intenses, CNRS-UGA-UPS-INSA-EMFL, 25 avenue des Martyrs, 38042 Grenoble, France*
[2]*Institute of Experimental Physics, Faculty of Physics, University of Warsaw, ul. Pasteura 5, 02-093 Warszawa, Poland*
[3]*Department of Experimental Physics, Faculty of Fundamental Problems of Technology, Wrocław University of Science and Technology, 27 Wybrzeże Wyspiańskiego, 50-370 Wrocław, Poland*
[4]*National Institute for Materials Science, 1-1 Namiki, Tsukuba 305-0044, Japan*
[5]*Laboratoire de Physique et Modélisation des Milieux Condensés, Université Grenoble Alpes and CNRS, 25 avenue des Martyrs, 38042 Grenoble, France*

(Received 1 February 2019; published 30 August 2019)

Monolayers of semiconducting transition metal dichalcogenides are two-dimensional direct-gap systems which host tightly bound excitons with an internal degree of freedom corresponding to the valley of the constituting carriers. Strong spin-orbit interaction and the resulting ordering of the spin-split subbands in the valence and conduction bands makes the lowest-lying excitons in WX_2 (X being S or Se) spin forbidden and optically dark. With polarization-resolved photoluminescence experiments performed on a WSe_2 monolayer encapsulated in a hexagonal boron nitride, we show how the intrinsic exchange interaction in combination with the applied in-plane and/or out-of-plane magnetic fields enables one to probe and manipulate the valley degree of freedom of the dark excitons.

DOI: 10.1103/PhysRevLett.123.096803

Monolayers (MLs) of semiconducting transition metal dichalcogenides (TMDs), such as MX_2 with $M =$ Mo or W, and $X =$ S, Se, or Te, are two-dimensional direct-gap semiconductors [1] which attract a lot of interest due to their unique physical properties and potential applications in optoelectronics, photonics, and the development of valleytronics [2–7]. The direct band gap in S-TMD MLs is located at the two inequivalent $\mathbf{K}_\pm$ points (valleys) of the first Brillouin zone, related by time reversal symmetry. In MLs, the optically bright excitons [8–11] from $\mathbf{K}_\pm$ valley can efficiently couple to light with right or left circular polarization[12,13], respectively.

A unique feature of S-TMD monolayers is the so-called spin-valley locking [13]: strong spin-orbit interaction lifts the degeneracy between the two spin projections $s = \uparrow, \downarrow$ in each valley, leaving only the Kramers degeneracy between the opposite valleys, $\mathbf{K}_+, s \leftrightarrow \mathbf{K}_-, -s$. While the valence band (VB) spin-orbit splitting Δ_v is very large (several hundred meV [13]), its conduction band (CB) counterpart Δ_c is by an order of magnitude smaller [14–18], thus allowing some degree of manipulation by an in-plane magnetic field. In tungsten-based S-TMDs, Δ_c has the same sign as Δ_v, leading to the spin subband ordering shown in Fig. 1(a). In each valley, the optically bright exciton has a higher energy than the dark exciton which is composed of the conduction and valence electronic states with opposite spin projections. This results in a strong temperature

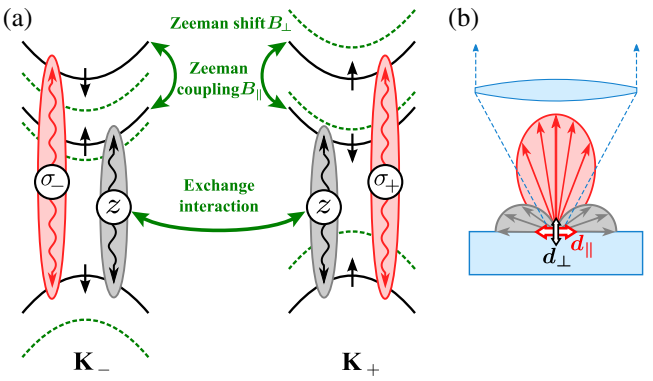

FIG. 1. (a) Spin and valley structure of WSe_2. Black curves show the spin-split bands in the $\mathbf{K}_\pm$ valleys at zero magnetic field, the spin projections are indicated by black arrows. Grey (red) ellipses represent spin-forbidden (spin-allowed) excitonic transitions in each valley. Dashed green curves show Zeeman-shifted bands in a perpendicular magnetic field. Thick green arrows represent the exchange interaction which mixes the two valleys, and the Zeeman coupling in an in-plane magnetic field which mixes different spin subbands in the same valley. (b) A schematic representation of radiation patterns of dark and bright excitons in a ML at zero magnetic field. The grey (red) arrows indicate the propagation direction of the light, emitted by dark (bright) excitons. The blue dashed lines define the region of light collected by the lens. The black and red double-headed arrows depict the directions of out-of-plane ($d_\perp$) and in-plane ($d_\parallel$) dipoles.

dependence of the photoluminescence (PL) efficiency, as the bright states become more populated at higher temperatures [19–21].

Dark excitons can couple to light only via a residual spin-flip dipole matrix element $d_\perp$, whose direction is perpendicular to the ML plane [22–24]. In consequence, the emission of dark excitons is directed predominantly along the ML plane, in contrast to the out-of-plane emission of bright excitons characterized by strong in-plane optical dipoles, $d_\parallel$, see Fig. 1(b). Notably, the valley degeneracy of dark excitons is lifted by the exchange interaction which mixes the valleys and produces two eigenstates with different energies. The higher energy component takes up the whole oscillator strength due to $d_\perp$ (we call it "grey"), while the low-energy component is completely decoupled from light and truly "dark" [23,25].

The possibility to control the valley degree of freedom for bright excitons by optical polarization [26–28] and external magnetic field [29–31] is impaired by the quick valley relaxation due to the exchange interaction [22,32], because the latter (i) depends on the exciton center-of-mass momentum, and (ii) is considerably strong, being governed by the same (large) in-plane dipole moment $d_\parallel$ as the optical transitions. For dark excitons, the exchange interaction is (i) a short-range local field effect, so it weakly depends on momentum, (ii) strong enough to produce a sizeable dark- grey splitting $\delta \approx 0.6$ meV ≈ 7 K in WSe_2 [33] which makes the dark component dominant at low temperatures, and (iii) at the same time weak enough to enable a control of the splitting and of the valley content by a perpendicular magnetic field $B_\perp$ of a few Tesla [33]. Importantly, by applying an in-plane magnetic field $B_\parallel$, one can transfer the in-plane oscillator strength from the higher-energy bright states to the dark-grey doublet [17,18], thus boosting the out-of-plane emission of light from both components of this doublet.

In this Letter, we present an experimental implementation of the described "dark exciton valley toolkit" in a WSe_2 ML. Namely, we experimentally demonstrate the coherent valley-superposition nature of the dark and grey excitons by transferring the oscillator strength from the bright excitons with an in-plane magnetic field and detecting a linearly polarized luminescence. We use a WSe_2 sample encapsulated in hexagonal boron nitride (hBN) [34–38]. In our experiment, the encapsulation leads to a strong brightening effect, much more pronounced than observed earlier [17,18], and enables us to spectrally resolve the fine structure of the dark excitons. We observed that the combination of the in-plane and out-of-plane magnetic fields leads to circularly polarized emissions due to the dark and grey excitons.

The valley structure of intravalley excitons in a magnetic field of arbitrary orientation can be described using the model of Refs. [17,23,33]. Let us work in the basis of the four intravalley A-exciton states with zero center-of-mass momentum at zero magnetic field. These states $|\mathbf{K}_\pm, s_c\rangle$ can be identified by the valley $\mathbf{K}_\pm$ and the CB spin projection $s_c = \uparrow, \downarrow$. The VB spin projection is fixed for the A exciton: $s_v = \uparrow$ in $\mathbf{K}_+$ valley and $\downarrow$ in $\mathbf{K}_-$. The states $|\mathbf{K}_+, \uparrow\rangle$, $|\mathbf{K}_-, \downarrow\rangle$ are bright and are denoted by $|\mathbf{K}_\pm, b\rangle$, respectively. Their transition dipole matrix elements lie in the plane and correspond to the two circular polarizations, $\langle 0|\hat{\mathbf{d}}|\mathbf{K}_\pm, b\rangle = -id_\parallel(\pm\mathbf{e}_x + i\mathbf{e}_y)$. The states $|\mathbf{K}_+, \downarrow\rangle$, $|\mathbf{K}_-, \uparrow\rangle$ are denoted as $|\mathbf{K}_\pm, d\rangle$ and have transition dipoles $\langle 0|\hat{\mathbf{d}}|\mathbf{K}_\pm, d\rangle = id_\perp \mathbf{e}_z$, perpendicular to the plane [22–24,33,39].

In the basis $|\mathbf{K}_+, b\rangle$, $|\mathbf{K}_-, b\rangle$, $|\mathbf{K}_+, d\rangle$, $|\mathbf{K}_-, d\rangle$, the Hamiltonian matrix has the form

$$H = \begin{bmatrix} \Delta + g_b\mathcal{B}_z & 0 & g_\parallel\mathcal{B}_- & 0 \\ 0 & \Delta - g_b\mathcal{B}_z & 0 & g_\parallel\mathcal{B}_+ \\ g_\parallel\mathcal{B}_+ & 0 & \delta/2 + g_d\mathcal{B}_z & \delta/2 \\ 0 & g_\parallel\mathcal{B}_- & \delta/2 & \delta/2 - g_d\mathcal{B}_z \end{bmatrix}. \tag{1}$$

Counting energies from the dark exciton state, we denoted by $\Delta \approx 40$ meV [17,18,24,33] and $\delta \approx 0.6$ meV [33], respectively, the dark-bright and dark-grey splitting at zero field. The parameter δ characterizes the short-range exchange interaction which lifts the valley degeneracy of the dark excitons at $B_\perp = 0$ and forms two new (grey and dark) eigenstates: $|G\rangle, |D\rangle = (|\mathbf{K}_+, d\rangle \pm |\mathbf{K}_-, d\rangle)/\sqrt{2}$.

Other terms in Eq. (1) describe the effect of the magnetic field, of the in-plane component, $B_\parallel$, and of the perpendicular one, $B_\perp$; we use the shorthand notation $\mathcal{B}_z \equiv \mu_B B_\perp/2$, $\mathcal{B}_\pm \equiv \mu_B(B_x \pm iB_y)/2$, where μ_B is the Bohr magneton. The field $B_\perp$ lifts the single-electron Kramers degeneracy between opposite spins in opposite valleys. This results in a valley-dependent shift of the excitonic levels with different Landé factors in the bright and dark-grey sectors. The field $\mathbf{B}_\parallel = (B_x, B_y)$ produces the Zeeman coupling ($g_\parallel\mu_B B_\parallel$) of the electronic states with opposite spins in the same valley, and thus mixes the dark-grey and bright excitonic sectors, remaining diagonal in the valley index.

The magnetic field terms in the Hamiltonian [Eq. (1)] provide the experimental tools which enable one to control and probe the dark exciton states. At $B_\parallel = 0$, one can tune continuously the valley content of the dark and grey excitons by changing $B_\perp$. Then, turning on the $B_\parallel$ field, one admixes the bright states to the dark-grey sector, thereby transferring the in-plane oscillator strength; since Δ is the largest energy scale in the Hamiltonian [Eq. (1)], this admixture can be treated perturbatively. Then it turns out that the valley content of the eigenstates in the dark-grey sector can be probed by measuring linear polarization of the light emitted now in the direction perpendicular to the ML plane. Consider an eigenstate $|\psi_d\rangle$ at $B_\parallel = 0$ in the form of a

general linear combination, $|\psi_d\rangle = \chi_+ e^{i\phi_d}|\mathbf{K}_+, d\rangle + \chi_- e^{-i\phi_d}|\mathbf{K}_-, d\rangle$ with real $\chi_\pm$, $\chi_+^2 + \chi_-^2 = 1$ and some phase ϕ_d. Let us apply $B_\parallel$ and detect the luminescence, emitted normally to the plane, with an analyzer selecting the electric field direction with the polar angle ϕ_a. Then, calculating perturbatively in $1/\Delta$ the corresponding in-plane dipole matrix element, we obtain the emitted light intensity:

$$I_\perp(\phi_a) \propto \left(d_\parallel \frac{g_\parallel \mu_B B_\parallel}{\Delta}\right)^2 \times [(\chi_+ - \chi_-)^2 + 4\chi_+\chi_- \sin^2(\phi_a + \phi_d - \phi_B)], \quad (2)$$

where $\phi_B = \arctan(B_y/B_x)$ is the polar angle of the in-plane magnetic field. Below we present the experimental implementation of the described tools.

Figures 2(a)–2(c) illustrate the results of micro-magneto-PL measurements performed in a wide spectral range (1.64–1.71 eV), covering the whole emission spectrum of our sample with spectral resolution of 0.8 nm. In contrast, the results shown in Figs. 2(d) and 2(e) and in the inset of Fig. 2(a) refer to experiments with higher spectral resolution (0.1 nm). All spectra were measured in the configuration of the normal incidence of the excitation and the collected beams [see Fig. 1(b) and the Supplemental Material [40] for details]. The X^D and X^G peaks are ascribed, correspondingly, to dark and grey states of the neutral exciton. Only X^G is observed in the spectra measured at zero magnetic field. We expect that the X^G emission is directed predominantly along the ML plane, thought it is still visible in the spectra, due to a relatively high numerical aperture (NA) of the lenses used to collect the emitted light. Both components of the X^D/X^G doublet contribute to the emission spectrum when the magnetic field is applied [see, e.g., Fig. 2(d)]. Note that this doublet structure is not resolved in the spectra shown in Fig. 2(b), measured with low spectral resolution. These results are in good agreement with previous reports [24,33,35,42–45,55]: (i) the X^G line is red-shifted by

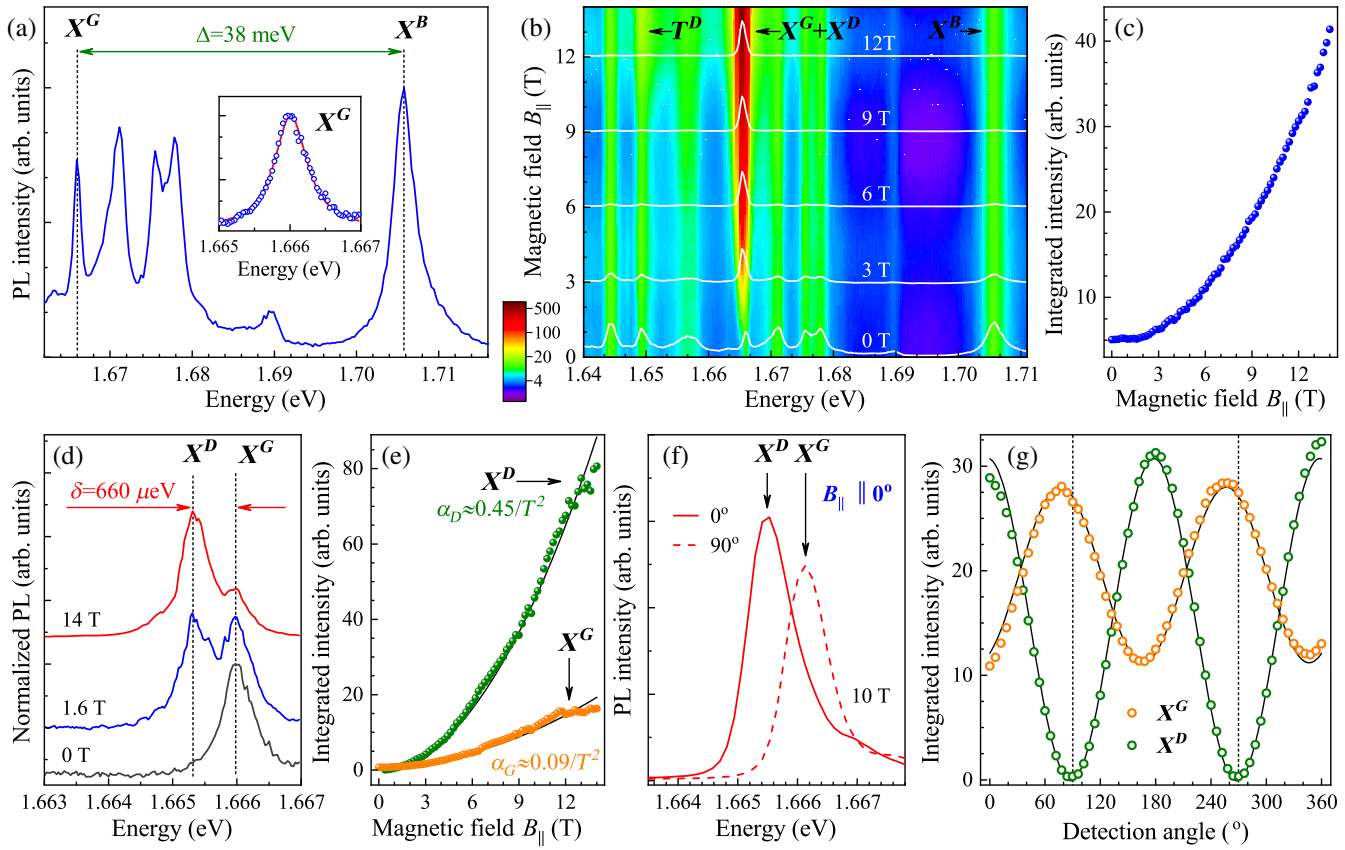

FIG. 2. (a) Low-temperature ($T = 4.2$ K) PL spectrum measured on a WSe_2 ML encapsulated in hBN flakes, using an excitation energy 2.408 eV and a power of 50 μW, and zero magnetic field. The inset shows the high-resolution PL emission of the grey exciton. (b) False-color map of the PL response as a function of $B_\parallel$; white curves superimposed on the map represent the PL spectra normalized to the most intense peaks recorded at selected values of $B_\parallel$. (c) Total emission as a function of $B_\parallel$ [frequency integral of panel (b)]. (d) High resolution PL spectra normalized to the most intense peaks at selected values of $B_\parallel$. (e) $B_\parallel$ dependence of the dark and grey exciton integrated intensities. The solid black curves represent quadratic fits. (f) PL spectra at $B_\parallel = 10$ T recorded for two orthogonal linear polarizations oriented parallel (solid curve) and perpendicular (dashed curves) to the direction of $\mathbf{B}_\parallel$ (excitation energy 1.917 eV and power 50 μW). (g) Polarization dependence of the dark and grey exciton integrated intensities measured at $B_\parallel = 10$ T.

38 meV from the emission peak X^B associated with the neutral bright exciton [see Fig. 2(a)]; (ii) the energy separation between the X^G and X^D excitons is $\delta = 660\ \mu$eV [see Fig. 2(d)]; (iii) the X^D and X^G lines are much narrower ($\simeq$0.6 meV) than the X^B line ($\simeq$4 meV), which indicates the significantly longer lifetimes of dark and grey excitons as compared to the lifetime of the bright exciton (see the Supplemental Material [40] for details).

Application of the in-plane magnetic field $B_\parallel$ leads to a strong brightening effect, which is remarkably pronounced in our encapsulated WSe_2 ML, much more than in previously probed WSe_2 MLs on Si/SiO_2 substrates [17,18]. This is demonstrated in Fig. 2(b) showing PL spectra measured in a wide spectral range, as a function of $B_\parallel$. With increasing $B_\parallel$, the intensity of the grey or dark exciton doublet (separate components not resolved) increases significantly, while the intensity of the bright exciton and of the lower energy features of the spectrum, stays practically at the same level. Note that the T^D line observed at about 1.65 eV in Fig. 2(b) becomes significantly brighter at the largest magnetic fields ($B > 10$ T). Recently, this peak was ascribed to the dark negatively charged exciton [47]. In Fig. 2(c), we plot the total emission intensity as a function of $B_\parallel$. At $B_\parallel = 14$ T, this emission intensity is enhanced by an order of magnitude and practically the whole luminescence of the sample is due to the dark or grey excitons doublet.

The PL response of our sample, measured with better spectral resolution, enabled us, for the first time, to resolve the magnetic brightening of the dark and grey components separately. As can be seen in Fig. 2(d), while only the grey exciton is observed when $B_\parallel = 0$, at fields above 1.6 T the X^D line becomes more intense. The $B_\parallel$ dependence of the intensity of each component is expected to be $I = I_0 + \alpha B_\parallel^2$ [17,18], where the zero-field intensity I_0 vanishes for the dark component but is nonzero and depends on the NA of the excitation or detection lens for the grey component. The results of the quadratic fit are shown in Fig. 2(e). The α parameter is different for the two components: $\alpha_D = 0.45\ \mathrm{T}^{-2}$, while $\alpha_G = 0.09\ \mathrm{T}^{-2}$. This large difference is explained by the difference in the populations of the two states: at temperature $T = 4.2$ K which corresponds to our experimental conditions, the population ratio is $e^{-\delta/k_BT} = 0.16$, in reasonable agreement with the measured ratio $\alpha_G/\alpha_D = 0.2$.

Now, one can investigate the polarization properties of magnetically brightened dark and grey excitons, see Fig. 2(f). We present in Fig. 2(g) the integrated PL intensity for each peak, as collected via the linear polarizer and measured as a function of the angle $\phi_a - \phi_B$ between the polarizer axis and the direction of the $\mathbf{B}_\parallel$ field. For the dark exciton, the polarization dependence fully agrees with Eq. (2): indeed, at $B_\perp = 0$, we have $\chi_+ = -\chi_- = 1/\sqrt{2}$ and $\phi_d = 0$, resulting in the transition dipole oriented along $\mathbf{B}_\parallel$. Our polarization measurement thus reveals experimentally the nature of the dark exciton state, which is a coherent superposition of the states in the two valleys.

For the grey exciton, the measured polarization dependence corresponds to Eq. (2) plus a constant background. The latter is due to large NA of the lens used to collect the emitted light. Indeed, Eq. (2) describes emission perpendicular to the ML and thus is valid in the limit of small NA. Our large-NA lens picks up the light emitted by the out-of-plane component $d_\perp$ of the transition dipole moment, which has no in-plane polarization. For the dark exciton at $B_\perp = 0$, this component is absent.

Application of a magnetic field $B_\perp$ shifts the energies in the two valleys in the opposite directions. Thus, the eigenstates in the dark-grey sector resulting from valley mixing by exchange coupling have no longer equal weights in the two valleys. As a result, both grey and dark exciton components have a finite out-of-plane optical dipole moment even at $B_\parallel = 0$, and are visible in the luminescence spectra due to large NA of the lens (see the Supplemental Material [40] for details). Note that the intensity of the dark exciton lines is independent of the detected helicity (σ_+ or σ_-) of light.

In order to induce the $\sigma_\pm$ selectivity for the dark excitons emission, we propose to combine the effects of $B_\parallel$ and $B_\perp$ magnetic fields. $B_\parallel$ gives rise to linear polarizations of the grey and dark excitons [see Figs. 2(f), 2(g)], and which are subsequently transformed by $B_\perp$ into elliptical polarizations. The experimental evidence corroborating this scenario is presented in Figs. 3(a)–3(c). Upon increasing of the $B_\perp$, both dark and grey excitons gain circular σ_+ and σ_- polarizations, respectively. This determines that the g factor of dark and grey excitons is negative. The gradual increase in the circular degree of polarization, illustrated in Figs. 3(a)–3(c), can be described in terms of the competition between the Zeeman shift $g_d\mu_B B_\perp$ and the initial splitting δ and taking into account a finite NA of excitation or collection lens. The result of such competition is presented in Fig. 3(d) for the case of dark exciton emission, as an example. The blue dots (red curve) depicts the experimentally (theoretically) derived data of the circular polarization degree as a function of field $B_\perp$. Note that the value of the polarization degree saturates already at 60% and not at 100% as one can expect. The explanation of such phenomenon involves a finite contribution of the out-of-plane dipole components of X^D and X^G exciton states (see the Supplemental Material [40] for details). To prove the dominant contribution of the circular polarization ($\sigma_\pm$) for the dark and grey exciton emissions, they were measured as a function of orientation of the $\lambda/4$ wave plate in detection, see Fig. 3(f).

In this Letter, we investigated the PL response of a hBN-encapsulated WSe_2 ML subject to a magnetic field, whose direction lies in the ML plane, or perpendicular to it. Thanks to the encapsulation, the in-plane field leads to a

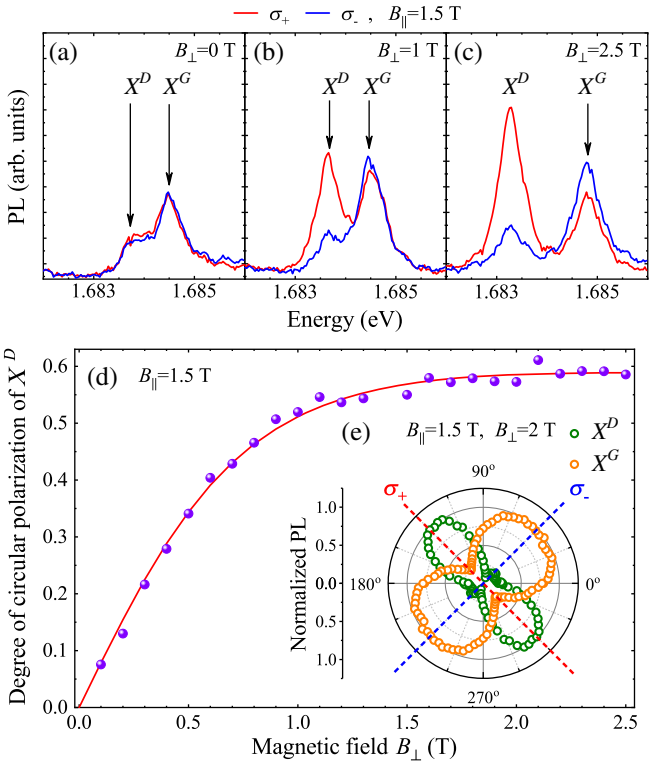

FIG. 3. (a)–(c) PL spectra of dark and grey excitons in perpendicular magnetic field applied additionally to in-plane magnetic field of 1.5 T. (d) Emergence of the circular polarization of the dark exciton upon application of additional perpendicular magnetic field. Solid red line represents a fit of function described in the Supplemental Material [40]. (e) PL intensity of X^D and X^G as a function of orientation of the $\lambda/4$ wave plate in detection. Settings 45° and 135° correspond to σ_- and σ_+ polarization, respectively. The data were measured for orientations 0–180° and cloned to 180–360° range for the sake of presentation. Note that these results where measured on a different sample as those shown in Fig. 2.

very pronounced brightening effect on the dark lowest-energy excitons in WSe_2, and most of the sample's luminescence comes from these dark excitons. In our encapsulated sample one can resolve the fine structure of the magnetically brightened dark excitons, split by the exchange interaction which produces two coherent valley superpositions as eigenstates. We were able to probe the coefficients of the superpositions by a polarization-resolved PL measurement. These coefficients can be changed by applying a perpendicular and/or parallel magnetic field. These findings open a perspective for controlled manipulation of the valley degree of freedom of long-lived dark excitons in monolayer S-TMDs.

The work has been supported by the ATOMOPTO project (TEAM programme of the Foundation for Polish Science, co-financed by the EU within the ERDFund), the EU Graphene Flagship project (No. 785219), the National Science Centre, Poland (Grant No. 2018/31/B/ST3/02111), the Nanofab facility of the Institut Néel, CNRS/UGA and the LNCMI-CNRS, a member of the European Magnetic Field Laboratory (EMFL). K. W. and T. T. acknowledge support from the Elemental Strategy Initiative conducted by the MEXT, Japan, and the CREST (JPMJCR15F3), JST.

*maciej.molas@fuw.edu.pl
†marek.potemski@lncmi.cnrs.fr

[1] K. F. Mak, C. Lee, J. Hone, J. Shan, and T. F. Heinz, Phys. Rev. Lett. **105**, 136805 (2010).
[2] Q. H. Wang, K.-Z. Kourosh, A. Kis, J. N. Coleman, and M. S. Strano, Nat. Nanotechnol. **7**, 699 (2012).
[3] G. Eda and S. A. Maier, ACS Nano **7**, 5660 (2013).
[4] F. Xia, H. Wang, D. Xiao, M. Dubey, and A. Ramasubramaniam, Nat. Photonics **8**, 899 (2014).
[5] X. Xu, W. Yao, D. Xiao, and T. F. Heinz, Nat. Phys. **10**, 343 (2014).
[6] M. Koperski, M. R. Molas, A. Arora, K. Nogajewski, A. O. Slobodeniuk, C. Faugeras, and M. Potemski, Nanophotonics **6**, 1289 (2017).
[7] G. Wang, A. Chernikov, M. M. Glazov, T. F. Heinz, X. Marie, T. Amand, and B. Urbaszek, Rev. Mod. Phys. **90**, 021001 (2018).
[8] A. Chernikov, T. C. Berkelbach, H. M. Hill, A. Rigosi, Y. Li, O. B. Aslan, D. R. Reichman, M. S. Hybertsen, and T. F. Heinz, Phys. Rev. Lett. **113**, 076802 (2014).
[9] Z. Ye, T. Cao, K. O'Brien, H. Zhu, X. Yin, Y. Wang, S. G. Louie, and X. Zhang, Nature (London) **513**, 214 (2014).
[10] M. M. Ugeda, A. J. Bradley, S.-F. Shi, F. H. da Jornada, Y. Zhang, D. Y. Qiu, W. Ruan, S.-K. Mo, Z. Hussain, Z.-X. Shen, F. Wang, S. G. Louie, and M. F. Crommie, Nat. Mater. **13**, 1091 (2014).
[11] K. He, N. Kumar, L. Zhao, Z. Wang, K. F. Mak, H. Zhao, and J. Shan, Phys. Rev. Lett. **113**, 026803 (2014).
[12] W. Yao, D. Xiao, and Q. Niu, Phys. Rev. B **77**, 235406 (2008).
[13] D. Xiao, G.-B. Liu, W. Feng, X. Xu, and W. Yao, Phys. Rev. Lett. **108**, 196802 (2012).
[14] K. Kośmider, J. W. González, and J. Fernández-Rossier, Phys. Rev. B **88**, 245436 (2013).
[15] A. Kormányos, G. Burkard, M. Gmitra, J. Fabian, V. Zólyomi, N. D. Drummond, and V. Fal'ko, 2D Mater. **2**, 022001 (2015).
[16] J. P. Echeverry, B. Urbaszek, T. Amand, X. Marie, and I. C. Gerber, Phys. Rev. B **93**, 121107(R)(2016).
[17] M. R. Molas, C. Faugeras, A. O. Slobodeniuk, K. Nogajewski, M. Bartos, D. M. Basko, and M. Potemski, 2D Mater. **4**, 021003 (2017).
[18] X.-X. Zhang, T. Cao, Z. Lu, Y.-C. Lin, F. Zhang, Y. Wang, Z. Li, J. C. Hone, J. A. Robinson, D. Smirnov, S. G. Louie, and T. F. Heinz, Nat. Nanotechnol. **12**, 883 (2017).
[19] A. Arora, M. Koperski, K. Nogajewski, J. Marcus, C. Faugeras, and M. Potemski, Nanoscale **7**, 10421 (2015).
[20] X.-X. Zhang, Y. You, S. Y. Frank Zhao, and T. F. Heinz, Phys. Rev. Lett. **115**, 257403 (2015).
[21] G. Wang, C. Robert, A. Suslu, B. Chen, S. Yang, S. Alamdari, I. C. Gerber, T. Amand, X. Marie, S. Tongay, and B. Urbaszek, Nat. Commun. **6**, 10110 (2015).

[22] M. M. Glazov, T. Amand, X. Marie, D. Lagarde, L. Bouet, and B. Urbaszek, Phys. Rev. B **89**, 201302(R) (2014).
[23] A. O. Slobodeniuk and D. M. Basko, 2D Mater. **3**, 035009 (2016).
[24] G. Wang, C. Robert, M. M. Glazov, F. Cadiz, E. Courtade, T. Amand, D. Lagarde, T. Taniguchi, K. Watanabe, B. Urbaszek, and X. Marie, Phys. Rev. Lett. **119**, 047401 (2017).
[25] H. Dery and Y. Song, Phys. Rev. B **92**, 125431 (2015).
[26] H. Zeng, J. Dai, W. Yao, D. Xiao, and X. Cui, Nat. Nanotechnol. **7**, 490 (2012).
[27] K. F. Mak, K. He, J. Shan, and T. F. Heinz, Nat. Nanotechnol. **7**, 494 (2012).
[28] A. M. Jones, H. Yu, N. J. Ghimire, S. Wu, G. Aivazian, J. S. Ross, B. Zhao, J. Yan, D. G. Mandrus, D. Xiao, W. Yao, and X. Xu, Nat. Nanotechnol. **8**, 634 (2013).
[29] G. Aivazian, Z. Gong, A. M. Jones, R.-L. Chu, J. Yan, D. G. Mandrus, C. Zhang, D. Cobden, W. Yao, and X. Xu, Nat. Phys. **11**, 148 (2015).
[30] G. Wang, X. Marie, B. L. Liu, T. Amand, C. Robert, F. Cadiz, P. Renucci, and B. Urbaszek, Phys. Rev. Lett. **117**, 187401 (2016).
[31] T. Smoleński, M. Goryca, M. Koperski, C. Faugeras, T. Kazimierczuk, A. Bogucki, K. Nogajewski, P. Kossacki, and M. Potemski, Phys. Rev. X **6**, 021024 (2016).
[32] K. Hao, G. Moody, F. Wu, C. K. Dass, L. Xu, C.-H. Chen, L. Sun, M.-Y. Li, L.-J. Li, A. H. MacDonald, and X. Li, Nat. Phys. **12**, 677 (2016).
[33] C. Robert, T. Amand, F. Cadiz, D. Lagarde, E. Courtade, M. Manca, T. Taniguchi, K. Watanabe, B. Urbaszek, and X. Marie, Phys. Rev. B **96**, 155423 (2017).
[34] Z. Wang, J. Shan, and K. F. Mak, Nat. Nanotechnol. **12**, 144 (2017).
[35] F. Cadiz, E. Courtade, C. Robert, G. Wang, Y. Shen, H. Cai, T. Taniguchi, K. Watanabe, H. Carrere, D. Lagarde, M. Manca, T. Amand, P. Renucci, S. Tongay, X. Marie, and B. Urbaszek, Phys. Rev. X **7**, 021026 (2017).
[36] O. A. Ajayi, J. V. Ardelean, G. D. Shepard, J. Wang, A. Antony, T. Taniguchi, K. Watanabe, T. F. Heinz, S. Strauf, X.-Y. Zhu, and J. C. Hone, 2D Mater. **4**, 031011 (2017).
[37] M. Manca, C. R. M. M. Glazov, T. T. F. Cadiz, E. C. K. Watanabe, P. R. T. Amand, G. W. X. Marie, and B. Urbaszek, Nat. Commun. **8**, 14927 (2017).
[38] D. Vaclavkova, J. Wyzula, K. Nogajewski, M. Bartos, A. O. Slobodeniuk, C. Faugeras, M. Potemski, and M. R. Molas, Nanotechnology **29**, 325705 (2018).
[39] A. O. Slobodeniuk and D. M. Basko, 2D Mater. **6**, 029501 (2019).
[40] See Supplemental Material at http://link.aps.org/supplemental/10.1103/PhysRevLett.123.096803 for description of the experimental details and the additional obtained results devoted to the properties of grey and dark excitons emissions, which includes Refs. [6,20,29,33,41–54].
[41] A. Castellanos-Gomez, M. Buscema, R. Molenaar, V. Singh, L. Janssen, H. S. J. van der Zant, and G. A. Steele, 2D Mater. **1**, 011002 (2014).
[42] E. Courtade, M. Semina, M. Manca, M. M. Glazov, C. Robert, F. Cadiz, G. Wang, T. Taniguchi, K. Watanabe, M. Pierre, W. Escoffier, E. L. Ivchenko, P. Renucci, X. Marie, T. Amand, and B. Urbaszek, Phys. Rev. B **96**, 085302 (2017).
[43] Z. Li, T. Wang, Z. Lu, C. Jin, Y. Chen, Y. Meng, Z. Lian, T. Taniguchi, K. Watanabe, S. Zhang, D. Smirnov, and S.-F. Shi, Nat. Commun. **9**, 3719 (2018).
[44] S.-Y. Chen, T. Goldstein, T. Taniguchi, K. Watanabe, and J. Yan, Nat. Commun. **9**, 3717 (2018).
[45] M. Barbone, A. R. P. Montblanch, D. M. Kara, C. Palacios-Berraquero, A. R. Cadore, D. De Fazio, B. Pingault, E. Mostaani, H. Li, B. Chen, K. Watanabe, T. Taniguchi, S. Tongay, G. Wang, A. C. Ferrari, and M. Atatüre, Nat. Commun. **9**, 3721 (2018).
[46] M. Paur, A. J. Molina-Mendoza, R. Bratschitsch, K. Watanabe, T. Taniguchi, and T. Mueller, Nat. Commun. **10**, 1709 (2019).
[47] E. Liu, J. van Baren, Z. Lu, M. M. Altaiary, T. Taniguchi, K. Watanabe, D. Smirnov, and C. H. Lui, Phys. Rev. Lett. **123**, 027401 (2019).
[48] C. Robert, D. Lagarde, F. Cadiz, G. Wang, B. Lassagne, T. Amand, A. Balocchi, P. Renucci, S. Tongay, B. Urbaszek, and X. Marie, Phys. Rev. B **93**, 205423 (2016).
[49] A. Srivastava, M. Sidler, A. V. Allain, D. S. Lembke, A. Kis, and A. Imamoglu, Nat. Phys. **11**, 141 (2015).
[50] G. Wang, L. Bouet, M. M. Glazov, T. Amand, E. L. Ivchenko, E. Palleau, X. Marie, and B. Urbaszek, 2D Mater. **2**, 034002 (2015).
[51] A. A. Mitioglu, P. Plochocka, Á. Granados del Aguila, P. C. M. Christianen, G. Deligeorgis, S. Anghel, L. Kulyuk, and D. K. Maude, Nano Lett. **15**, 4387 (2015).
[52] M. Koperski, M. R. Molas, A. Arora, K. Nogajewski, M. Bartos, J. Wyzula, D. Vaclavkova, P. Kossacki, and M. Potemski, 2D Mater. **6**, 015001 (2019).
[53] Y. Li, J. Ludwig, T. Low, A. Chernikov, X. Cui, G. Arefe, Y. D. Kim, A. M. van der Zande, A. Rigosi, H. M. Hill, S. H. Kim, J. Hone, Z. Li, D. Smirnov, and T. F. Heinz, Phys. Rev. Lett. **113**, 266804 (2014).
[54] D. MacNeill, C. Heikes, K. F. Mak, Z. Anderson, A. Kormányos, V. Zólyomi, J. Park, and D. C. Ralph, Phys. Rev. Lett. **114**, 037401 (2015).
[55] Y. Zhou, G. Scuri, D. S. Wild, A. A. High, A. Dibos, L. A. Jauregui, C. Shu, K. De Greve, K. Pistunova, A. Y. Joe, T. Taniguchi, K. Watanabe, P. Kim, M. D. Lukin, and H. Park, Nat. Nanotechnol. **12**, 856 (2017).